nature physics

Article

https://doi.org/10.1038/s41567-023-02270-6

Guiding Trojan light beams via Lagrange points

Received: 30 June 2023

Accepted: 25 September 2023

Published online: 3 January 2024

Check for updates

Haokun Luo [1,5], Yunxuan Wei [1,5], Fan O. Wu [2,3], Georgios G. Pyrialakos [1,2], Demetrios N. Christodoulides [1,4] ✉ & Mercedeh Khajavikhan [1,4] ✉

The guided transmission of optical waves is critical for light-based applications in modern communication, information processing and energy generation systems. Traditionally, the guiding of light waves in structures such as optical fibres has been predominantly achieved through the use of total internal reflection. In periodic platforms, a variety of other physical mechanisms can also be deployed to transport optical waves. However, transversely confining light in fully dielectric, non-periodic and passive configurations remains a challenge in situations where total internal reflection is not supported. Here we present an approach to trapping light that utilizes the exotic features of Lagrange points—a special class of equilibrium positions akin to those responsible for capturing Trojan asteroids in celestial mechanics. This is achieved in twisted arrangements in which optical Coriolis forces induce guiding channels even at locations where the refractive index landscape is defocusing or entirely unremarkable. These findings may have implications beyond standard optical waveguiding schemes and could also apply to other physical systems such as acoustics, electron beams and ultracold atoms.

Moulding the flow of light is nowadays one of the cornerstones of modern photonic technologies[1–6]. In this respect, in recent years there has been a flurry of intense activities on several research fronts such as those associated with topological[7–10] and non-Hermitian optics[10,11], photonic crystals[2–6,12], optical metamaterials[13,14] and metasurfaces[15,16]. Of crucial importance are methodologies by means of which light can be transmitted in a guided format. Perhaps the most prominent of them is that offered by optical fibres that are known to rely on the process of total internal reflection[1]. Unlike in fibres where light waves are trapped in a high-index region, in periodic photonic settings, waveguiding can also be attained through other mechanisms such as Bragg reflection[2–6,12,17,18], evanescent coupling[19] and bound states in the continuum effects[20]. Similarly, light can propagate in a confined manner in plasmonic[21] or active arrangements that allow gain guidance[22]. At this point, the following questions naturally arise. Will it be possible to guide light in a fully dielectric and passive material system without making use of either total internal reflection or periodicity? In a wider context, can guiding occur in an open or bulk space environment, where trapping is achieved through a remote mechanism that can act and be manipulated from afar? If so, a new paradigm is established through which not only light, but also other types of waves such as acoustic or electron beams, can be trapped by utilizing altogether new strategies.

In celestial mechanics, Lagrange points represent equilibrium positions whereby the gravitational attraction from two orbiting massive bodies balances the centrifugal force[23,24]. In this situation, one can identify five Lagrange points designated as L_1, L_2, …, L_5 with the first three (L_1, L_2 and L_3) being by nature unstable, whereas the remaining two (L_4 and L_5) are stable[23]. As a result, a small mass can be forever trapped in the vicinity of these two latter points, like, for example, the Trojan asteroids in the Sun–Jupiter system (Fig. 1a). Although, at first glance, the two-dimensional potential distribution within the co-rotating frame appears to be unstable around the $L_{4,5}$ points shown

[1]Ming Hsieh Department of Electrical and Computer Engineering, University of Southern California, California, CA, USA. [2]CREOL, The College of Optics and Photonics, University of Central Florida, Orlando, FL, USA. [3]School of Applied and Engineering Physics, Cornell University, Ithaca, NY, USA. [4]Department of Physics and Astronomy, University of Southern California, California, CA, USA. [5]These authors contributed equally: Haokun Luo, Yunxuan Wei. ✉e-mail: Demetri@usc.edu; khajavik@usc.edu

https://doi.org/10.1038/s41567-023-02270-6

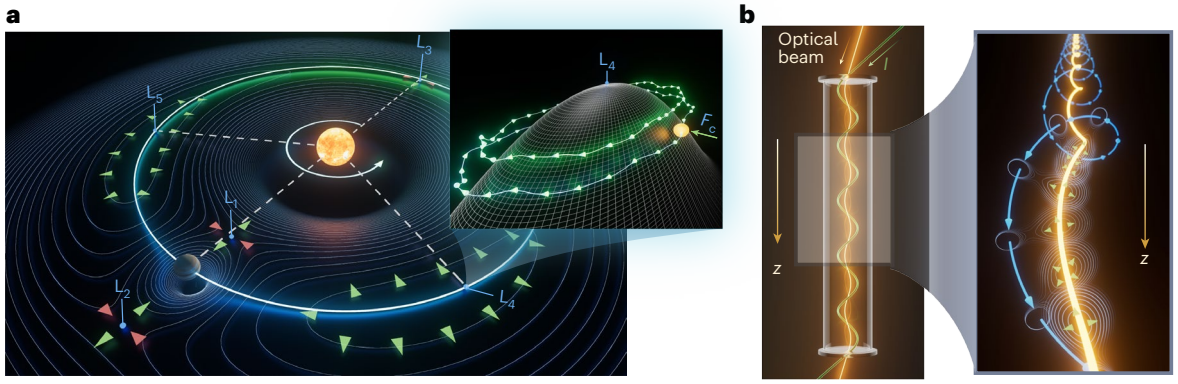

Fig. 1 | Celestial and optical beam dynamics in the vicinity of a stable Lagrange point. a, Lagrange points in the Sun–Jupiter system. In the co-rotating frame, the potentials associated with the three unstable colinear Lagrange points (L_1, L_2 and L_3) are saddle shaped, whereas those of L_4 and L_5 are stable, being maxima. The inset in **a** shows the stable trajectory of an asteroid when captured around an L_4 Lagrange point because of the Coriolis force. **b**, Experimental set-up used to observe optical Trojan bound states (bright yellow beam). A stable Lagrange point is established by means of the thermo-optic effect by passing current *I* through a helical iron wire (shown in green) embedded in a cured PDMS cylinder. The inset in **b** displays in a schematic manner the trapping of a Trojan beam (depicted in bright yellow) at a Lagrange point induced by a helicoidal index potential (blue line).

in Fig. 1a (given that it is concave downwards, as shown in Fig. 1a), counterintuitively, the motion of a third body can be dynamically stabilized because of the Coriolis force. In essence, as this body starts to roll down from the $L_{4,5}$ potential hill, the Coriolis force tends to continuously pull it back, which thus results in a bounded orbit (inset in Fig. 1a). In recent years, the analogue of this process has also been used in atomic physics to produce non-dispersive wavepackets[25–27], which is a prospect enabled by the isomorphism between the Coulomb force and the gravitational attraction.

In this work, we demonstrate a new approach for guiding light in transparent dielectric systems. This is achieved by exploiting the intriguing characteristics of the Lagrange points and the equivalence between the paraxial wave equation for light and the non-relativistic Schrödinger equation. The resulting optical Trojan beams can be captured even in defocusing environments at points where the refractive index profile (within the stationary frame) is totally ordinary—with no features that could foretell a guiding behaviour. We show that, in the optical domain, this mechanism can be established in a versatile manner through a variety of attractive and/or repulsive index potentials. Given that Newton's third law governing the dynamics of celestial bodies is, in our optical set-up, inconsequential in establishing a rotating potential, multiple Lagrange points can now be simultaneously generated at will in 'many-body' configurations, which is an aspect that is impossible in other settings.

Figure 1b depicts a schematic of the experimental arrangement used to observe optical Trojan beams. These beams are excited in ~30 cm long glass cylinders with a radius of $b = 1.18$ cm that are filled with cured polydimethylsiloxane (PDMS) of refractive index $n_0 = 1.46$. To produce optical Lagrange points, we exploit the large thermo-optic effect offered by PDMS ($\mathrm{d}n/\mathrm{d}T = -4.5 \times 10^{-4}\,\mathrm{K}^{-1}$). This is achieved by inserting a twisted iron wire (of radius $a = 275$ μm) in the tube before the PDMS is cured. An electric current is then passed through this wire which, in turn, heats the PDMS to induce a logarithmic defocusing spiral index potential (Supplementary Information Sections 1 and 2) through the thermo-optic process (Fig. 2a).

In addressing the prospect of trapping light at a Lagrange point, we consider, in the stationary coordinate system (x, y), the logarithmic defocusing index profile depicted in Fig. 2a, which is typical of that thermally produced in our experiments. This long-range potential is spiralling around the centre C with a pitch of $\Lambda = 8$ cm. In this example, the index contrast induced (with respect to the surface of the metallic wire) is approximately 2.25×10^{-2}. On the other hand, the same index potential remains static when viewed within the co-rotating frame, which is shown in Fig. 2b along with the corresponding iso-contour lines. In this frame, because of centrifugal effects, the effective potential is modified, which leads to two Lagrange points (designated as L_A and L_B) where the optical attraction or repulsion is balanced. In this case, it so happens that only L_A is stable whereas L_B is unstable. The position of L_A is also marked in Fig. 2a for clarity. To showcase the trapping potential of the Lagrange points, we begin our analysis by examining ray dynamics in the vicinity of L_A (Supplementary Information Section 3). Figure 2c shows the calculated ray trajectories, from where one can conclude that light is captured around this Lagrange point. As in the case of Trojan asteroids, here stability is introduced because of Coriolis forces. Interestingly, this is possible even though the potential is defocusing (and hence, repulsive) and it is produced by only one source, unlike the Sun–Jupiter system[23]. As indicated previously, the index landscape around the L_A point, when viewed within the stationary (x, y) system (Fig. 2a), happens to be completely ordinary, with no special features that could ever foretell that light can be trapped. The stability criteria for these optical Lagrange points are provided in Supplementary Information Section 4.

Although the ray dynamics do suggest that light can be guided at a Lagrange point, it is still imperative to formally assert this possibility within the framework of wave optics. To do so, we use the paraxial wave equation, which is a reduced form of the Helmholtz electromagnetic problem in weakly guiding arrangements and so happens to be isomorphic to the Schrödinger equation. In normalized units, this is given by $\mathrm{i}\partial_z\psi = \hat{H}\psi$ where $\hat{H} = -(\partial_{xx} + \partial_{yy})/2 + V(x, y, z)$ is the Hamiltonian operator and ψ is the slowly varying electric field amplitude. The potential $V(x, y, z)$ that appears in the Hamiltonian is directly proportional to the refractive index profile (Supplementary Information Section 5). The paraxial equation can be more conveniently studied within the co-rotating frame (u, v, ξ) after a 'magnetic' vector potential $\mathbf{A}$ is introduced by means of $\mathbf{A} = \boldsymbol{\Omega} \times \mathbf{r}$ to account for optical Coriolis effects[8,28], where $\Omega = 2\pi/\Lambda$ is the rotation rate. In this case, by keeping in mind that $\xi = z$, the optical beam evolution equation takes the form

$$\mathrm{i}\frac{\partial\psi}{\partial z} = \left[\frac{1}{2}(\mathbf{p} - \mathbf{A})^2 + V_{\Omega,\mathrm{eff}}(u, v)\right]\psi, \tag{1}$$

where $\mathbf{p} = -\mathrm{i}\hat{u}\partial/\partial u - \mathrm{i}\hat{v}\partial/\partial v$ and $V_{\Omega,\mathrm{eff}}(u, v) = V(u, v) - \Omega^2 r^2/2$ (Supplementary Information Section 6). Equation (1) is solved numerically to identify bound modes in the form of $\psi = \mathrm{e}^{\mathrm{i}\sigma z} R(u, v)\,\mathrm{e}^{\mathrm{i}\Psi(u,v)}$ centred

https://doi.org/10.1038/s41567-023-02270-6

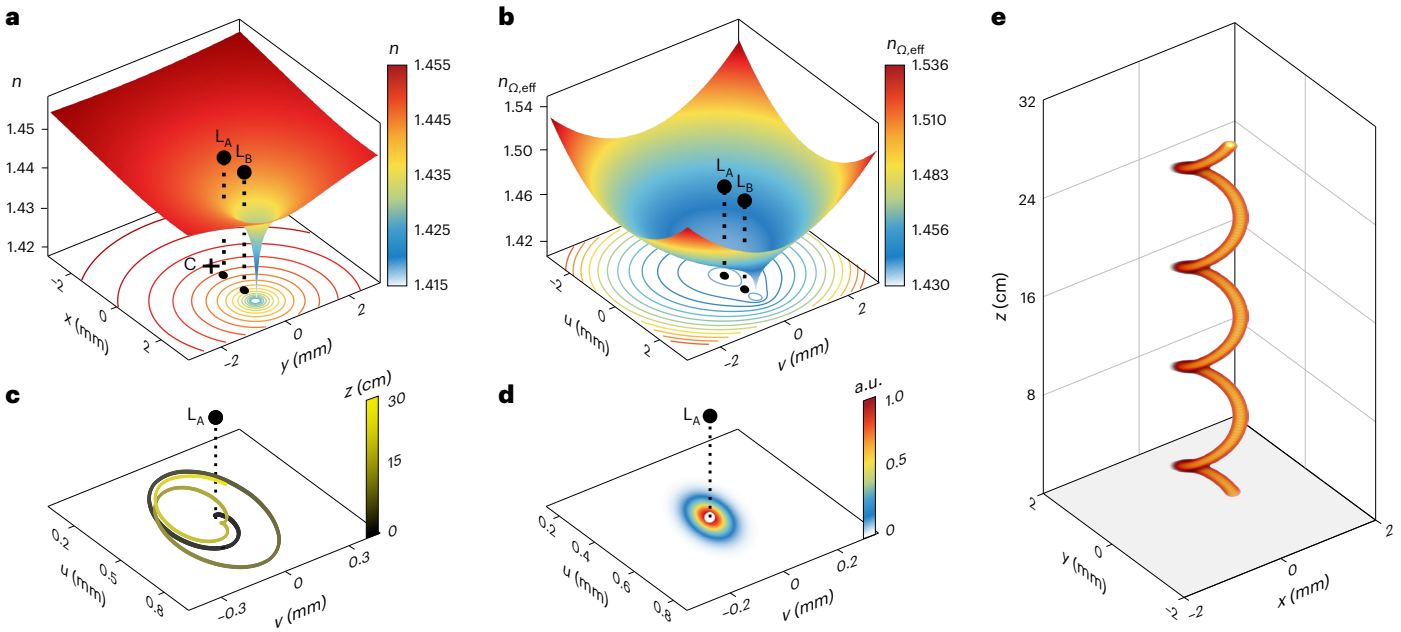

Fig. 2 | Light propagation dynamics around a stable Lagrange point. a, An induced logarithmic defocusing spiralling index potential when viewed within the stationary frame (x, y). This index profile rotates along z at a constant angular velocity Ω around the centre C. The corresponding iso-contour lines are also shown. **b**, In the co-rotating frame (u, v), the effective index potential now involves centrifugal effects and exhibits two Lagrange points, L_A and L_B. L_B is a saddle point and hence is unstable. On the other hand, L_A exhibits a minimum where the dynamics can be stabilized through the optical Coriolis force. Note that, in optics, the effective index distribution in the co-rotating coordinate system is $\Delta n_{\Omega,\text{eff}} \propto -V_{\Omega,\text{eff}}$ (Supplementary Information Section 4). For comparison, the positions of L_A and L_B are also marked in **a**. **c**, Stable ray dynamics unfolding around L_A in the index landscape depicted in **a** and **b** as viewed within in the co-rotating frame. **d**, Numerically obtained normalized intensity distribution in arbitrary units (a.u.) for the fundamental Trojan optical mode centred at L_A, corresponding to **a** and **b**. In this case, the mode is elliptical in the (u, v) system. **e**, Stable propagation of the optical Trojan ground state shown in **d**, as obtained from numerically solving equation (1) along z. The beam remains invariant along its helical path. The helix pitch in **a**–**e** is $\Lambda = 8$ cm.

at a stable Lagrange point, where σ denotes their corresponding eigenvalue. Figure 2d depicts the intensity profile of the ground state associated with the L_A point in Fig. 2b. In this case, the intensity of the fundamental Trojan mode is elliptical, as one would expect given that the index potential around L_A has approximately an elliptic paraboloidal dependence. The propagation characteristics of the Trojan beam are then numerically investigated within the stationary (x, y) frame (Fig. 2e). Evidently, being a mode, the Trojan beam remains invariant during propagation while twisting around the centre point C. In other words, because of Coriolis forces, the beam is stably trapped around the Lagrange point, and thus overcomes any diffraction and attraction and/or repulsion effects. These results are in accordance with those obtained from ray dynamics. The correspondence between wave and ray optics can be directly established through the Ehrenfest theorem (Supplementary Information Section 7).

To observe Trojan beams, experiments were conducted in PDMS filled cylinders (Fig. 1b). The optical dynamics of these beams were monitored both at the output facet of the cylinder as well as from the side using an imaging camera. To enable side-view observations, the PDMS was mixed with a small amount of titanium dioxide (TiO_2) nanoparticles (165 nm in diameter). In this experiment, the spiral iron wire was positioned at 1.85 mm from the centre C, having a pitch $\Lambda = 8$ cm. The Trojan mode was then excited by a Gaussian beam with a spot size of $w_0 \simeq 110$ μm from a He–Ne laser ($\lambda_0 = 632.8$ nm), right at the Lagrange point of this arrangement. A direct current $I = 4.0$ A was passed through the wire to heat the sample. In this case, the surface of the wire was estimated to be at 50 K above the outer surface temperature of the cylinder and the resulting temperature distribution led to a spiralling logarithmic index potential $\Delta n \simeq -2.25 \times 10^{-2}[1 - \ln(\rho/a)/\ln(b/a)]$, where ρ is the distance from the wire centre (Supplementary Information Section 2). In this configuration, the Lagrange point L_A was positioned ~430 μm away from the centre C. Experiments demonstrating that the Trojan beam was captured around L_A are shown in Fig. 3a,b, which demonstrate that, indeed, the beam retained its spot size both at the output facet (Fig. 3b) and during propagation (Fig. 3b). At the output, the mean value of the spot size radius was ~112 μm with an ellipticity of 0.49. The variation of the average beam spot size as a function of distance and current is depicted in Fig. 3c,d. If the current was turned off, the beam was no longer trapped and finally expanded after ~30 cm of propagation to $w \simeq 385$ μm because of diffraction (Fig. 3e,f). Next, we kept the wire straight while conveying the same current $I = 4.0$ A. Interestingly, in this scenario, not only was the beam diffracted but it was also strongly repelled by the defocusing (repulsive) index potential and forced into a self-bouncing trajectory at the boundary of the cylinder (Fig. 3g). This response confirms that the Lagrange point was responsible for the behaviour displayed in Fig. 3a,b.

To demonstrate in a definitive manner that what is observed in our set-up is a Trojan beam, we experimentally detected its phase structure that so happens to be quite unique to this trapped state. To explain the origin and importance of this phase $\Psi(u, v)$, we approximately represent the effective potential landscape in the vicinity of a Lagrange point (u_i, v_i) where it is maximum by means of a Taylor series. In this case, one can obtain closed form solutions for the bound states of equation (1) (Supplementary Information Section 8), from which we find that $\Psi(u, v) = \alpha u + \beta v + \gamma uv$. The first two terms (α, β) are associated with the tilt of the Trojan beam when traversing its helical path and the last term γuv governs the internal energy flow that allows this elliptical state to reorient itself during propagation. We would like to emphasize that the γuv phase is unique to these Trojan entities, given that it does not appear in standard dielectric waveguide settings or gain-guiding systems. Numerical simulations carried out for the index profiles used in our experiments (Fig. 2b), lead to similar results

https://doi.org/10.1038/s41567-023-02270-6

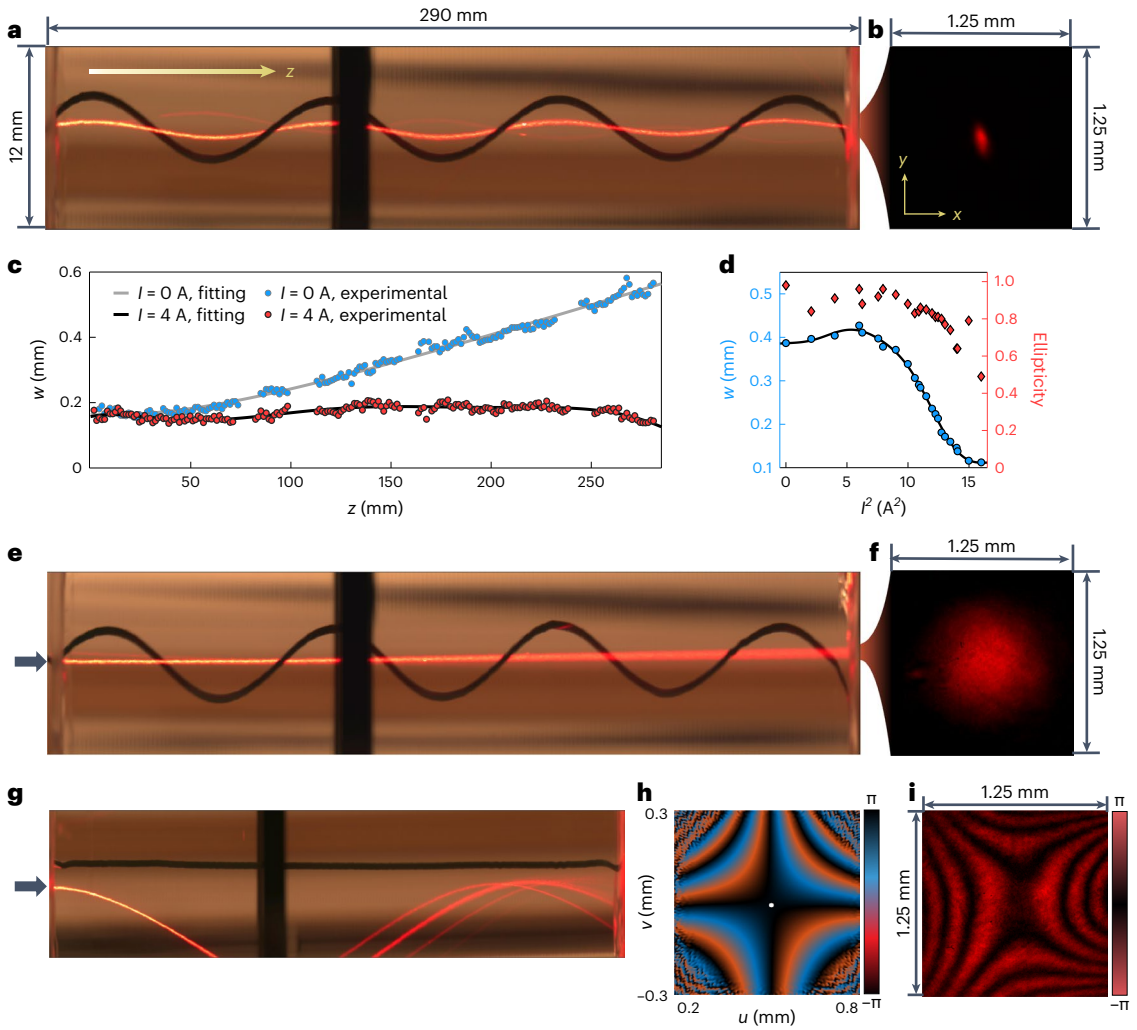

Fig. 3 | Trojan beam guiding in the index potential produced by a single helical heat source. a, Side-view image of the trapped fundamental Trojan mode (red beam) when helicoidally traversing a PDMS filled tube. The spiralling wire, carrying a current $I = 4.0$ A, is also shown in the background. The spot size of the Gaussian beam at the input is ~110 µm. **b**, Intensity profile of the Trojan mode at the output facet, after a distance of approximately 30 cm. The mean value of the spot size radius is ~112 µm with an ellipticity of 0.49 (minor/major axis). **c**, Variation of the beam's mean spot size as a function of distance for $I = 4.0$ A. **d**, Dependence of the Trojan mode's output mean spot size and ellipticity versus current I^2. **e**, Side-view image of the diffraction dynamics of the input Gaussian beam when the current is turned off. **f**, For the case shown in **e**, the circular beam diffracts to a spot size of ~385 µm. **g**, When the wire is kept straight while carrying a current $I = 4.0$ A, the light beam is strongly repelled by the defocusing index landscape, which leads to self-bouncing behaviour at the surface of the cylinder. **h**, Numerically obtained phase structure associated with the fundamental Trojan mode centred around L_A (depicted as a white dot). The presence of the characteristic X-shaped γuv term is evident. **i**, Experimentally observed wavefront phase of the Trojan state corresponding to **a** and **b** detected by means of interferometry. The aspect ratio of **a** and **e** is 4.5:1 while that of **g** is 3.2:1. The dark stripe shown in **a**, **e** and **g** arises from the tube holder.

(Fig. 3h). To detect the γuv phase, we performed interferometric measurements using a Mach–Zehnder arrangement where the Trojan beam in one of the arms was appropriately tilted to remove the effects from the $(\alpha u + \beta v)$ contributions. The resulting X-shaped interferogram (produced by the γuv term) is shown in Fig. 3i. This provides irrefutable evidence that what was observed in our set-up was a Trojan beam. In optical arrangements, it is possible to excite multiple Lagrange points from several potential sources, which is something that is not feasible in celestial mechanics because many-body systems are chaotic (Supplementary Information Section 9). We would like to emphasize that what is discussed here is fundamentally different from results previously obtained in transversely periodic arrangements whereby diffraction effects can be arrested even in defocusing potentials by exploiting the effective diffraction properties (effective mass) of Bloch modes within the Brillouin zone[29,30]. On the other hand, in bulk media where the magnitude and sign of the diffraction cannot be altered, there is no other mechanism known (apart from the one presented in this work) by means of which light trapping is possible even in defocusing environments.

We next conducted experiments in a double-helix wire configuration when embedded in a cured PDMS cylinder. In this case, the Lagrange point was located right at the centre C. Each one of the two spiral wires was positioned at 1.8 mm from the centre C and the helix pitch used was $\Lambda = 6.3$ cm. When no current was flowing through the system, the optical beam diffracted to a spot size $w \simeq 375$ µm after ~30 cm of propagation (Fig. 4a,b). On the other hand, after a current $I = 3.5$ A was passed through the two wires (connected in series), an elliptical Trojan state was formed when excited with a Gaussian beam of spot size $w_0 \simeq 110$ µm (Fig. 4c,d). Our results clearly indicate that the beam was trapped around the Lagrange point given that, at the output, its mean spot size radius was approximately 120 µm with an ellipticity of 0.9 (Fig. 4d). The dependence of the average beam spot size on distance is depicted in Fig. 4e. The X-shaped interferogram resulting from the corresponding γuv phase is depicted in Fig. 4f. Experiments were also performed when

https://doi.org/10.1038/s41567-023-02270-6

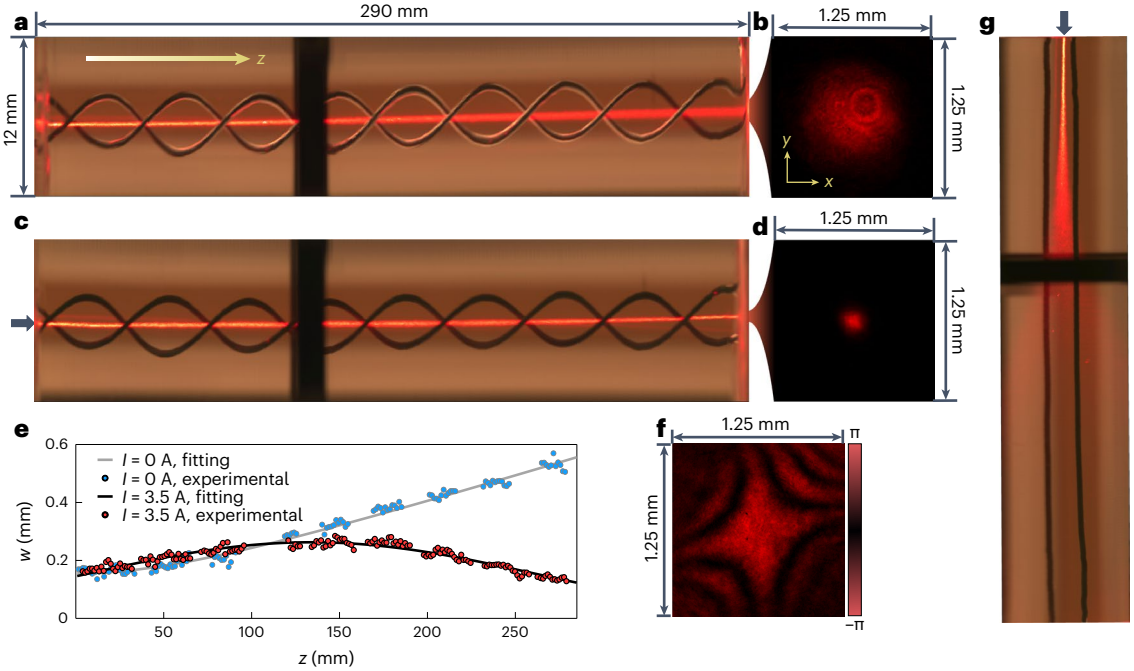

Fig. 4 | Trojan beam trapping in the index landscape produced by a double-helix current source. a, A Gaussian beam with a spot size of ~110 µm is injected into the sample when the current is $I = 0$ A. **b**, After ~30 cm of propagation the beam diffracts to a spot size of 375 µm. **c**, A Trojan optical mode was established when the current $I = 3.5$ A. In this case, the Lagrange point was located at the centre of this double-helix wire system ($\Lambda = 6.3$ cm). **d**, Output intensity profile of this Trojan state having a mean spot size of ~120 µm with an ellipticity of 0.9. **e**, Variation of the beam's mean spot size as a function of distance for $I = 3.5$ A. **f**, Interferometrically observed phase structure of the trapped mode shown in **c** and **d**, which is indicative of the X-shaped phase term. **g**, No Lagrange point is induced when the wires are kept straight and therefore the beam diffracts. The aspect ratio in **a**, **c** and **g** is 4.5:1. The dark stripe shown in **a**, **c** and **g** arises from the tube holder.

the two wires were kept straight, in which case no Lagrange point was produced (Fig. 4g). To some extent, trapping light in this double-helix arrangement is reminiscent of charged particle confinement in Paul traps[31,32] which is achieved by means of parametric interactions—a stabilization process that is nonetheless different from the one mediated by the Coriolis force.

In conclusion, we have demonstrated a new methodology for trapping light by utilizing the unique features of Lagrange points. The resulting Trojan beams can be guided even in defocusing refractive index landscapes because of optical Coriolis effects. This is enabled through their unique phase distribution that allows their internal energy to be appropriately rearranged along their trajectory. Our work may open new avenues in guiding optical waves in settings where traditional approaches are not possible, for example, in liquid environments. Of interest would be to investigate the possibility of observing these Trojan states in amplifying configurations where optical gain can exert long-range attractive or repulsive forces on a signal that is not confined in a standard dielectric waveguide. The prospect of guiding and deflecting light at Lagrange points induced by orbiting ultra-massive bodies such as black holes or neutron stars can be another exciting direction in astrophysics.

Online content

Any methods, additional references, Nature Portfolio reporting summaries, source data, extended data, supplementary information, acknowledgements, peer review information; details of author contributions and competing interests; and statements of data and code availability are available at https://doi.org/10.1038/s41567-023-02270-6.

References

1. Snyder, A. W. & Love, J. D. *Optical Waveguide Theory* (Springer, 1983).
2. Knight, J. C. Photonic crystal fibres. *Nature* **424**, 847–851 (2003).
3. Birks, T. A., Knight, J. C. & Russell, P. S. J. Endlessly single-mode photonic crystal fiber. *Opt. Lett.* **22**, 961–963 (1997).
4. Ibanescu, M., Fink, Y., Fan, S., Thomas, E. L. & Joannopoulos, J. D. An all-dielectric coaxial waveguide. *Science* **289**, 415–419 (2000).
5. Joannopoulos, J. D., Villeneuve, P. R. & Fan, S. Photonic crystals: putting a new twist on light. *Nature* **386**, 143–149 (1997).
6. Yeh, P., Yariv, A. & Marom, E. Theory of Bragg fiber. *J. Opt. Soc. Am.* **68**, 1196–1201 (1978).
7. Bandres, M. A. et al. Topological insulator laser: experiments. *Science* **359**, eaar4005 (2018).
8. Rechtsman, M. C. et al. Photonic Floquet topological insulators. *Nature* **496**, 196–200 (2013).
9. Wimmer, M., Price, H. M., Carusotto, I. & Peschel, U. Experimental measurement of the Berry curvature from anomalous transport. *Nat. Phys.* **13**, 545–550 (2017).
10. Weidemann, S. et al. Topological funneling of light. *Science* **368**, 311–314 (2020).
11. Rüter, C. E. et al. Observation of parity–time symmetry in optics. *Nat. Phys.* **6**, 192–195 (2010).
12. Yablonovitch, E. Inhibited spontaneous emission in solid-state physics and electronics. *Phys. Rev. Lett.* **58**, 2059–2062 (1987).
13. Shalaev, V. M. Optical negative-index metamaterials. *Nat. Photon.* **1**, 41–48 (2007).
14. Engheta, N. & Ziolkowski, R. W. *Metamaterials: Physics and Engineering Explorations* (Wiley, 2006).
15. Arbabi, A., Horie, Y., Bagheri, M. & Faraon, A. Dielectric metasurfaces for complete control of phase and polarization with subwavelength spatial resolution and high transmission. *Nat. Nanotechnol.* **10**, 937–943 (2015).
16. Kildishev, A. V., Boltasseva, A. & Shalaev, V. M. Planar photonics with metasurfaces. *Science* **339**, 1232009 (2013).

17. Freedman, B. et al. Grating-mediated wave guiding and holographic solitons. *J. Opt. Soc. Am. B* **22**, 1349–1355 (2005).
18. Habib, M. S., Antonio-Lopez, J. E., Markos, C., Schülzgen, A. & Amezcua-Correa, R. Single-mode, low loss hollow-core anti-resonant fiber designs. *Opt. Express* **27**, 3824–3836 (2019).
19. Yariv, A., Xu, Y., Lee, R. K. & Scherer, A. Coupled-resonator optical waveguide: a proposal and analysis. *Opt. Lett.* **24**, 711–713 (1999).
20. Hsu, C. W., Zhen, B., Stone, A. D., Joannopoulos, J. D. & Soljačić, M. Bound states in the continuum. *Nat. Rev. Mater.* **1**, 16048 (2016).
21. Brongersma, M. L. & Kik, P. G. *Surface Plasmon Nanophotonics* (Springer, 2007).
22. Siegman, A. E. Propagating modes in gain-guided optical fibers. *J. Opt. Soc. Am. A* **20**, 1617–1628 (2003).
23. Bannikova, E. & Capaccioli, M. *Foundations of Celestial Mechanics* (Springer, 2022).
24. Pérez-Villegas, A., Portail, M., Wegg, C. & Gerhard, O. Revisiting the tale of Hercules: how stars orbiting the Lagrange points visit the Sun. *Astrophys. J. Lett.* **840**, L2 (2017).
25. Bialynicki-Birula, I., Kaliński, M. & Eberly, J. H. Lagrange equilibrium points in celestial mechanics and nonspreading wave packets for strongly driven Rydberg electrons. *Phys. Rev. Lett.* **73**, 1777–1780 (1994).
26. Kalinski, M. & Eberly, J. H. New states of hydrogen in a circularly polarized electromagnetic field. *Phys. Rev. Lett.* **77**, 2420–2423 (1996).
27. Buchleitner, A., Delande, D. & Zakrzewski, J. Non-dispersive wave packets in periodically driven quantum systems. *Phys. Rep.* **368**, 409–547 (2002).
28. Mueller, E. J., Ho, T.-L., Ueda, M. & Baym, G. Fragmentation of Bose–Einstein condensates. *Phys. Rev. A* **74**, 033612 (2006).
29. Longhi, S. Bloch dynamics of light waves in helical optical waveguide arrays. *Phys. Rev. B* **76**, 195119 (2007).
30. Beravat, R., Wong, G. K. L., Frosz, M. H., Xi, X. M. & Russell, P. S. J. Twist-induced guidance in coreless photonic crystal fiber: a helical channel for light. *Sci. Adv.* **2**, e1601421 (2016).
31. Paul, W. Electromagnetic traps for charged and neutral particles. *Rev. Mod. Phys.* **62**, 531–540 (1990).
32. Harari, G., Ben-Aryeh, Y. & Mann, A. Propagator for the general time-dependent harmonic oscillator with application to an ion trap. *Phys. Rev. A* **84**, 062104 (2011).

Methods

Experimental optical set-up

The experimental set-up comprised three main characterization components. These included: (1) beam excitation; (2) side-view imaging; and (3) bottom-view imaging and interference. For exciting a beam, a linearly polarized He–Ne laser (Thorlabs HNL050LB) operating at a wavelength of 632.8 nm was used. Its output Gaussian beam was ×5 expanded through a 4*f* system and then focused to a spot size of $w_0 \simeq 110$ μm at the input facet through a convex focusing lens C_f having a focal length of F_{C_f}. To acquire a side view of the beam dynamics inside the tube, a complementary metal oxide semiconductor (CMOS) camera (EO-1312c, Edmund Inc.) was used in conjunction with a lens, and was attached to a vertically movable stage along the propagation direction. A microscope, involving a ×10 objective (numerical aperture = 0.28) and an $F = 125$ mm lens, was employed to image the transverse profile of the Trojan beam at the bottom facet. Interferometric measurements were performed by splitting the light after the microscope into two arms, the first one passing through a ×2.86 4*f* system to expand it into a flat wavefront whereas the other one was appropriately attenuated to perform the interferometric measurement. A linear polarizer was inserted into the reference arm to adjust the interference contrast. The interference pattern was finally projected with a magnification ×0.5 on to a CMOS camera through a 4*f* system. The spatial frequency spectra of the two interfering beams were matched at the focal plane of the $F = 200$ mm lens in this 4*f* system so that the tilt phase shift terms (α, β) were eliminated by tilting the reference beam. In imaging the optical beam profiles at the output facet (collected by a CMOS camera (BladeCam-HR, Dataray Inc.)), both the reference arm and the attenuator were removed. The details are provided in Supplementary Information Section 1.

In characterizing the phase structure of the Trojan beams, the focal length of the C_f lens was changed depending on the current *I* used. This was done to observe the phase structure by expanding the intensity distribution that further facilitated the interferometric measurements. The focal lengths of the C_f for different currents *I* are provided in Supplementary Information Section 1.

In addition to the camera lens providing approximately ×0.4, the magnification of the side-view system was also affected by the circular interface between air and the PDMS filled glass tube. Given that the refractive indices of glass ($n_{glass} = 1.457$) and PDMS ($n_0 \approx 1.46$) are approximately the same, then, under paraxial conditions, the magnification was exactly 1.46 when the object was placed at the centre of the tube (Supplementary Information Section 1). This inherent magnification was taken into account when estimating the beam spot size from side-view imaging.

Sample preparation

Our sample involved a spiralling iron wire surrounded by cured PDMS in an ~30-cm-long glass tube. The tube was covered by two transparent acrylic discs to avoid dealing with curved surfaces arising from surface tension and any other distortion effects from thermal expansion. The radius of the iron wire was $a = 0.275$ mm, and the outer and inner radii of the glass tube were $b_{outer} = 15.0$ mm and $b = 11.8$ mm, respectively. A direct current source was connected to the helical iron wire embedded in the cured PDMS, for heating and generating the required logarithmic twisted refractive index potential. To image the optical beams from the side, a small amount of TiO_2 nanoparticles (165 nm in diameter (Nanomaterials Inc.)) were uniformly distributed in PDMS (Microlubrol Sylcap 284-F) as scatterers. Typical samples used in single- and double-helix wire configurations are provided in Supplementary Information Section 1.

Ray stability analysis around a Lagrange point

The stability of ray dynamics around a stable Lagrange point located at (u_i, v_i) was analysed. In the co-rotating (u, v) system, the potential landscape in the vicinity of this point was locally a maximum: that is, to first order, its Taylor series was given by $V_{\Omega,\mathrm{eff}} = -\Delta n_{\Omega,\mathrm{eff}}(u,v)/n_0 = V_{\max} - (\omega_1^2(u-u_i)^2 + \omega_2^2(v-v_i)^2)/2$. If we let $\tilde{u} = u - u_i, \tilde{v} = v - v_i$, the equations governing the ray dynamics (Supplementary Information Section 4) are given

$$\ddot{\tilde{u}} = 2\Omega\dot{\tilde{v}} + \omega_1^2\tilde{u}, \tag{2-1}$$

$$\ddot{\tilde{v}} = -2\Omega\dot{\tilde{u}} + \omega_2^2\tilde{v}. \tag{2-2}$$

By solving the corresponding eigenvalue problem (Supplementary Information Section 4), one finds that the ray trajectories around the Lagrange point are stable only when

$$2\Omega > \omega_1 + \omega_2 \tag{3}$$

Equation (3) provides the stability criterion required to trap an optical ray around a stable Lagrange point.

Analytical solution for the fundamental Trojan mode in a twisted parabolic potential

Here we provide an analytical solution for the fundamental Trojan mode in a twisted parabolic elliptical potential. The Lagrange point was located at (u_i, v_i) within the (u, v) system. To do so, we first obtained this solution when the potential was shifted to the centre, in which case, to first order, $V_{\Omega,\mathrm{eff}} = V_{\max} - (\omega_1^2u^2 + \omega_2^2v^2)/2$. In this case, the optical envelope obeys

$$\begin{aligned} \mathrm{i}\frac{\partial\psi}{\partial z} = &-\frac{1}{2}\left(\frac{\partial^2\psi}{\partial u^2} + \frac{\partial^2\psi}{\partial v^2}\right) + \mathrm{i}\Omega\left(u\frac{\partial\psi}{\partial v} - v\frac{\partial\psi}{\partial u}\right) \\ &+ \frac{1}{2}\Omega^2(u^2+v^2)\psi + \left(V_{\max} - \frac{(\omega_1^2u^2+\omega_2^2v^2)}{2}\right)\psi. \end{aligned} \tag{4}$$

The ground state of equation (4) has the form of an elliptical Gaussian function[33]

$$\psi = N\mathrm{e}^{-pu^2}\mathrm{e}^{-qv^2}\mathrm{e}^{\mathrm{i}\gamma uv}\mathrm{e}^{\mathrm{i}\sigma z}\mathrm{e}^{-\mathrm{i}V_{\max}z}, \tag{5}$$

where $p, q > 0$ $(p, q \in \mathcal{R}^+)$ and N is a normalization factor. The parameters involved in this solution are given in (Supplementary Information Section 8)

$$\gamma = \frac{\omega_2 - \omega_1}{\omega_2 + \omega_1}\Omega, \tag{6}$$

$$p = \frac{\left[4\Omega^2 - (\omega_1+\omega_2)^2\right]^{\frac{1}{2}}}{2(\omega_1+\omega_2)}\omega_1, \tag{7}$$

$$q = \frac{\left[4\Omega^2 - (\omega_1+\omega_2)^2\right]^{\frac{1}{2}}}{2(\omega_1+\omega_2)}\omega_2. \tag{8}$$

$$\sigma = -\frac{\left[4\Omega^2 - (\omega_1+\omega_2)^2\right]^{\frac{1}{2}}}{2} \tag{9}$$

Note that this solution is only possible if $2\Omega > \omega_1 + \omega_2$, which is identical to equation (3). This solution can be translated to (u_i, v_i) using a gauge phase[34], that is, $\psi_{u_i,v_i} = \psi(u-u_i, v-v_i)\mathrm{e}^{\mathrm{i}\Phi(u,v)}$, where $\Phi(u,v) = \Omega(u_iv - v_iu)$.

The dynamics of the Trojan mode can be solved numerically under any arbitrary initial conditions using a beam propagation method that relies on fast Fourier transforms. The Trojan modes supported by the

actual effective potential around a stable Lagrange point (such the one depicted in Fig. 2b) are obtained by numerically solving equation (1). In this case, the eigenvalue problem is solved using finite-difference methods.

Data availability

Source data are provided with this paper. All other data that support the plots within this paper and other findings of this study are available from the corresponding author upon reasonable request.

Code availability

The used numerical codes are based upon MATLAB and COMSOL and are available upon reasonable request to the corresponding authors.

References

33. Rebane, T. K. Two-dimensional oscillator in a magnetic field. *J. Exp. Theor. Phys.* **114**, 220–225 (2012).
34. Landau, L. D. & Lifshitz, E. M. in *Quantum Mechanics* 3rd edn (Ed. Pitavskii, L. P.) 453–471 (Pergamon, 1977).

Acknowledgements

This work was supported by the Air Force Office of Scientific Research (AFOSR) Multidisciplinary University Research Initiative (MURI) award on Novel light-matter interactions in topologically non-trivial Weyl semimetal structures and systems (award no. FA9550-20-1-0322) (M.K., D.N.C., H.L., Y.W., F.O.W. and G.G.P.), AFOSR MURI award on Programmable systems with non-Hermitian quantum dynamics (award no. FA9550-21-1-0202) (M.K., D.N.C., H.L., Y.W., F.O.W. and G.G.P.), ONR MURI award on the classical entanglement of light (award no. N00014-20-1-2789) (M.K., D.N.C., H.L., Y.W., F.O.W. and G.G.P.), AFRL – Applied Research Solutions (S03015) (FA8650-19-C-1692) (M.K.), W.M. Keck Foundation (D.N.C.), MPS Simons collaboration (Simons grant no. 733682) (D.N.C.) and US Air Force Research Laboratory (FA86511820019) (D.N.C.).

Author contributions

D.N.C. and M.K. conceived the idea. H.L., Y.W., F.O.W. and G.G.P. developed the theory. H.L. and Y.W. conducted the simulations, data analysis and the experiments. All the authors contributed to the writing of the original draft, reviewing and editing.

Inclusion and ethics

All authors acknowledge the Global Research Code on the development, implementation and communication of this research. For the purpose of transparency, we have included this statement on inclusion and ethics. This work cites a comprehensive list of research from around the world on related topics.

Competing interests

The authors declare no competing interests.

Additional information

Supplementary information The online version contains supplementary material available at https://doi.org/10.1038/s41567-023-02270-6.

Correspondence and requests for materials should be addressed to Demetrios N. Christodoulides or Mercedeh Khajavikhan.

Peer review information *Nature Physics* thanks Ulf Leonhardt and Tomáš Tyc for their contribution to the peer review of this work.